eTransportation 26 (2025) 100466

Contents lists available at ScienceDirect

eTransportation

journal homepage: www.journals.elsevier.com/etransportation

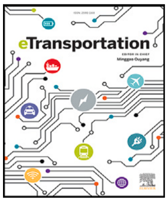

Advancing SOC estimation in $LiFePO_4$ batteries: Enhanced dQ/dV curve and short-pulse methods

Yizhao Gao, Simona Onori [*]

Department of Energy Science and Engineering, Stanford University, Stanford, CA 94305, USA

ARTICLE INFO

Keywords:
$LiFePO_4$ batteries
SOC estimation
DQV curves
UKF

ABSTRACT

Accurate state-of-charge (SOC) estimation for lithium iron phosphate ($LiFePO_4$) batteries remains challenging due to their inherently flat open-circuit voltage (OCV)–SOC characteristics, which impair observability for conventional voltage-based and equivalent circuit model (ECM) methods. To address this limitation, we propose a DQV-based SOC estimation framework that uses short-duration current pulses to extract informative voltage features. Complete DQV–SOC reference curves are constructed offline across multiple C-rates (± 1/30C, ± 0.2C, ± 0.5C, ± 1C, and ± 2C). During operation, voltage responses from brief current pulses are processed via exponential fitting to generate smooth, noise-resilient DQV segments. These segments are fused with the reference data within an Unscented Kalman Filter (UKF), enabling closed-loop SOC estimation with low computational overhead. Experimental results highlight the significant influence of C-rates on the DQV-based SOC estimator. We observe that pulse currents significantly enhance SOC estimation convergence across the full SOC range [0, 1]. However, employing a single C-rate pulse may not ensure robustness across diverse SOC ranges, emphasizing the importance of carefully selecting C-rates to achieve SOC estimation convergence throughout the entire SOC range of [0, 1]. This research contributes to advancing reliable management practices for $LiFePO_4$ batteries in electric vehicles.

1. Introduction

Lithium iron phosphate ($LiFePO_4$, referred as LFP) batteries are gaining prominence in electric vehicles (EVs) due to their superior thermal stability and cost-effectiveness compared to other lithium-ion technologies [1,2]. Effective management of these batteries necessitates a battery management system (BMS), as real-time monitoring is crucial to ensure safety and performance [3]. A critical function of the BMS is to estimate battery state-of-charge (SOC), which is vital for optimizing battery operation [4]. SOC, representing the charge level relative to capacity, is typically estimated from current, voltage, and temperature measurements [5]. However, SOC estimation for LFP batteries is particularly challenging due to the flat open-circuit voltage (OCV) characteristic, which introduces significant uncertainty when using OCV-based methods [6,7].

In recent years, numerous methods for estimating SOC in LFP batteries have been developed to address the challenge posed by the flatness of their OCV [8]. These methods can be grouped into three categories: equivalent-circuit model (ECM)-based, electrochemical-model-based, and machine-learning-based approaches.

ECM-based methods, including Extended Kalman filter (EKF) and Unscented Kalman filter (UKF), are based on the OCV-SOC relationship which plays a pivotal role in battery model-based SOC estimators [9,10]. In [11], a SOC estimation method for LFP-NMC hybrid batteries was proposed leveraging NMC cells as a reference to estimate SOC in LFP cells based on electricity equivalence in series cells. It integrates a difference state observer with fuzzy logic for continuous SOC correction, ensuring robustness against self-discharge differences and sensor errors. In [12], SOC estimation for LFP batteries is tackled through an adaptive strategy that dynamically adjusts EKF parameters based on OCV ranges by integrating the adaptive recursive square root algorithm for real-time OCV identification. The method is validated using large-scale real-world and laboratory data. To address OCV flatness and hysteresis effects, a covariance-controlled SOC estimator incorporating a simplified hysteresis model was introduced [13]. This approach enhances SOC accuracy by linearizing OCV hysteresis and dynamically adjusting EKF measurement error covariance, improving both convergence speed and robustness. A joint PID observer and improved adaptive extended Kalman filter was proposed for SOC estimation in LFP batteries, integrating a temperature compensation factor and an enhanced whale optimization algorithm to improve accuracy across different temperatures [14]. For hysteresis modeling, an advanced

---

[*] Corresponding author.
E-mail address: sonori@stanford.edu (S. Onori).

https://doi.org/10.1016/j.etran.2025.100466
Received 8 May 2025; Received in revised form 29 August 2025; Accepted 31 August 2025
Available online 11 September 2025

Nomenclature

Abbreviation	Definition
LFP	Lithium Iron Phosphate ($LiFePO_4$)
BMS	Battery Management System
ECM	Equivalent Circuit Model
SOC	State of Charge
EV	Electric Vehicle
OCV	Open Circuit Voltage
UKF	Unscented Kalman Filter
EKF	Extended Kalman Filter
DQV	Differential Capacity Curve

piecewise linearization method was developed to reduce approximation errors in OCV hysteresis contours [15]. It integrates EKF with Auto Regressive Exogenous modeling and Recursive Least Squares filtering for parameter estimation, improving estimation accuracy. A data-driven approach was introduced to construct OCV-SOC curves using real-world data [16] based on a segmentation-based OCV extraction technique.

A simplified mechanistic model was proposed for SOC estimation in LFP batteries by representing ion diffusion, polarization, and electrochemical reactions as a function of SOC [17]. In [18], a boundary observer was proposed, addressing the challenge of tracking lithium concentration and the moving interface position in the single particle model (SPM). By leveraging the backstepping method for partial differential equations of the lithium-ion diffusion, the proposed approach eliminates the impractical assumption of direct interface measurement, enhancing SOC estimation accuracy. An augmented physics-based model incorporating an empirical hysteresis component was presented in [19], where an UKF was integrated with a reduced-order electrochemical model.

For machine-learning-based techniques, a robust SOC estimation method for LFP batteries integrating a dynamic neural network with the Sage-Husa adaptive Kalman filter was presented in [20]. The method effectively captures the flat voltage curve nonlinearity and temperature sensitivity using an optimized Nonlinear Autoregressive Network with exogenous inputs. Another method introduces a deep learning-based approach using 10-min charging data to estimate SOC. This method combines a deep neural network with a Kalman filter to enhance noise robustness and utilizes transfer learning for adaptation to different battery types and aging conditions [21]. A SOC estimation method for LFP batteries was developed combining Coulomb counting reset, machine learning, and relaxation voltage analysis in [22]. It addresses SOC initialization challenges using low-frequency voltage data from short rest periods. Machine-learning-based algorithms require extensive experimental data for training, and their prediction capability heavily relies on the quality of the training dataset. Insufficient or biased data can lead to poor model performance and inaccurate SOC estimation [23]. Despite recent advances, existing SOC estimation methods continue to face significant challenges when applied to LFP batteries—particularly due to poor observability in the flat voltage plateau region, which limits estimation accuracy.

Differential capacity analysis, defined as the rate of change of charge with voltage (DQV), is a widely utilized technique for investigating electrode degradation mechanisms during charge or discharge processes [24]. The evolution of the area, location, and amplitude of DQV peaks and valleys provides valuable insights closely linked to battery aging [25]. Battery health indicators extracted from the peaks and valleys of partial incremental capacity curves contribute to battery health diagnosis [26,27]. While DQV analysis is commonly employed for battery diagnostics [28], its application in cell SOC estimation remains rarely seen.

In [29], a high-rate charging SOC estimation method was proposed based on the full incremental capacity curve, where DQV curves were filtered, segmented, and fitted with simple functions to establish DQV-SOC relationships. This approach enables accurate, real-time SOC estimation under fast-charging conditions without relying on complex models. In [30], a differential voltage analysis-based method was developed to estimate the remaining discharge capacity under dynamic conditions. Derived from electrochemical principles and validated using a pseudo-two-dimensional model (P2D), this method directly estimates the remaining discharge capacity from differential voltage analysis. Finally, in [31], incremental capacity analysis and differential voltage analysis were used, where three robust feature points were identified from these curves and quantitatively correlated with SOC and capacity.

In practical applications, low C-rate pulse currents and resulting voltage responses are sensitive to measurement noise [32,33]. Moreover, the robustness and effectiveness of combining pulse-current profiles with DQV curves have not been fully explored, highlighting the need for further research in this area to advance SOC estimation methodologies.

A critical gap identified through the literature review is the lack of investigation into a design framework of short-pulse current profiles for SOC estimation, as well as robustness and effectiveness of integrating pulse-current profiles with DQV curves for SOC estimation. Low C-rate pulse currents generate DQV curves with more pronounced valleys and peaks compared to high C-rate, however, their sensitivity to measurement noise poses a challenge. To date, no prior study has formulated SOC estimation for LFP batteries using a state-space framework with DQV curves as output. This work fills that gap by introducing a novel DQV-based state-space model, enhancing observability and enabling robust estimation despite the flat OCV–SOC characteristic.

The primary objective of this paper is to introduce a novel approach to SOC estimation for LFP batteries by shifting the focus from the traditional flat OCV-SOC relationship to a newly constructed output based on DQV curve: The key contributions of this paper are outlined below:

(1) State-Space framework for enhanced observability. We introduce a novel state-space model that uses DQV curves as measurement outputs to overcome the poor observability caused by the flat OCV–SOC profile in LFP batteries.
(2) Pulse Current profile design for SOC estimation. Short-duration current pulses at various C-rates are carefully designed, and exponential fitting is applied to extract accurate DQV features from noisy voltage responses.
(3) UKF-based SOC estimation: SOC estimations are made through a UKF, using the filtered DQV from the pulse response. This ensures stable and accurate predictions, even with the challenges of flat OCV-SOC characteristics in LFP batteries.

To aid the reader in understanding the overall structure and motivation of this work, Fig. 1 presents a high-level system diagram of the proposed framework. It summarizes the core challenge addressed—namely, the poor SOC observability in LFP cells—and highlights how the DQV technique, combined with pulse excitation and UKF-based estimation, enables robust and accurate SOC tracking.

2. Experimental setup and design of experiments

In this section, the experimental setup and experimental data collection process are elaborated. The cell testing platform is depicted in Fig. 2. Details of the battery testing equipment can be found in [34]. Six cells are placed in the AMEREX IC500R thermal chamber and are cycled using the Arbin LBT21024. The specifications of the LFP cell used in this study are listed in Table 1. Two sets of experiments were conducted in this study, all performed at a controlled temperature of 25 °C.

The first group of experiments involve the full discharge and charge of the cells at constant current rates of ±1/30C, ±0.2C, ±0.5C, ±1C,

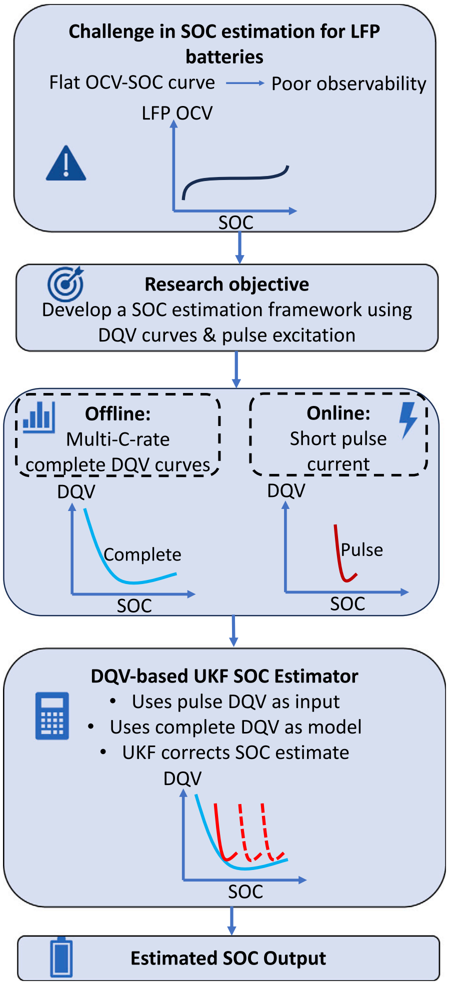

Fig. 1. Overview of the proposed DQV-based SOC estimation framework.

and ±2C, as depicted in Fig. 3 (– for discharge and + for charge). The charge and discharge voltages from constant current C-rates versus SOC are plotted in Fig. 3a and b, respectively. During the charging process, the cells are charged from a fully discharged state, starting when the voltage reaches the lower cut-off limit (0% SOC), and continues until they reach the upper voltage limit. Conversely, in the discharging process, the cells discharge from 100% SOC as the voltage starts at the upper limit and continues until it reaches the lower cut-off voltage. For the 1/30C baseline experiments, cells were charged from 0% to 100% SOC and then discharged back to 0% SOC at a constant current of 1/30C. The resulting voltage and capacity profiles were used to compute the complete DQV curves at +1/30C (charge) and –1/30C (discharge). For the C-rate experiments at higher currents, cells underwent two protocols: In the charging protocol, cells were first discharged from 100% to 0% SOC and then recharged to 100% SOC at the specified C-rate. In the discharging protocol, cells were charged from 0% to 100% SOC and then discharged back to 0% SOC using the same C-rate. These experimental voltage and current data were used to obtain complete DQV curves across the investigated C-rates. The resulting complete DQV curves serve as benchmarks for the DQV-based SOC estimator.

The second set of experiments is designed to validate the DQV-based SOC estimator using short-pulse currents at various SOC values. Figs. 4 and 5 show current and voltage data obtained from pulse tests conducted at constant current rates of ±1/30C, ±0.2C, ±0.5C, ±1C, and ±2C. In Fig. 4a, a charge current is applied for 720 s from 0% SOC, increasing the SOC by 16%. After a 10-min rest, five sequential 1/30C charge pulses, each lasting 1800 s and followed by a 300-s rest, are applied at increasing SOC levels, labeled as *a-e*. Similarly, in Fig. 4b, a discharge current is applied for 720 s from 100% SOC, decreasing the SOC by 16%. After a 10-min rest, five 1/30C discharge pulses are applied under the same conditions, also labeled as *a–e*.

Table 1
26650 cylindrical LFP cell specifications.

Nominal capacity	2.5 Ah
Nominal voltage	3.3 V
Lower voltage limit	2.0 V
Upper voltage limit	3.65 V
Cathode chemistry	$LiFePO_4$
Anode chemistry	Graphite

Fig. 4c and d depict charge and discharge pulse tests using a 0.2C current for 1800 s. In Fig. 4c, charging starts from 0% SOC, followed by a 7200-s rest, with ten charge pulses at progressively higher SOC levels, labeled *a–j*. In Fig. 4d, discharging starts from 100% SOC, followed by a 7200-s rest, with eleven discharge pulses labeled *a–k*. For the ±0.5C, ±1C, and ±2C pulse tests in Fig. 5, the procedure follows the ±0.2C tests but with adjusted pulse durations: 720 s for 0.5C, 360 s for 1C, and 180 s for 2C. These tests are designed to evaluate the DQV-SOC estimator's performance under different SOC conditions, and pulse current magnitude and duration. The SOC ranges for all pulses are summarized in Tables 2 and 3. The primary design criterion for the pulse duration was to achieve a consistent SOC excursion of approximately 10% per pulse. First, selecting a 10% SOC interval allows the pulse tests to cover the full SOC range (0%–100%) with a manageable number of pulses (approximately 10). Second, a 10% SOC change per pulse produces a voltage profile to capture identifiable and meaningful pulse DQV for estimation, while avoiding excessively long pulses.

3. SOC estimation framework utilizing pulse-current DQV data

The SOC estimation framework based on DQV data derived from pulse currents is structured in three parts. Part A generates complete DQV–SOC curves at various C-rates from constant-current experiments and stores them as lookup tables. Part B extracts DQV values from filtered voltage responses to short-duration current pulses. Part C employs a UKF-based observer that estimates SOC by minimizing the error between pulse DQV and the reference DQV curves. This framework enhances observability in LFP batteries and enables accurate SOC estimation across a broad range of operating conditions.

3.1. Algorithm part A: Complete DQV curve generation

The first part of the algorithm consists in generating the complete DQV curves as a function of SOC, referred to as $DQV_{complete}(SOC)$ across various C-rates (±1/30C, ±0.2C, ±0.5C, ±1C, and ±2C), as illustrated in Fig. 6. These DQV curves are then stored in DQV-SOC lookup tables for on-line use. The current, voltage, and temperature of the battery are measured with a sampling interval Δt of 1 s in this study. The discrete-time formulation of Coulomb counting is:

$$SOC\,(t+1) - SOC\,(t) = \frac{Q\,(t+1)}{Q_{capacity}} - \frac{Q\,(t)}{Q_{capacity}} = \frac{\Delta t}{3600 \cdot Q_{capacity}} I(t), \quad t = [1, 2, \ldots, N]. \tag{1}$$

where $SOC(t+1)$ and $SOC(t)$ represent the state of charge at the next and current time steps, respectively, N is the total number of data points, $Q(t+1)$ and $Q(t)$ denote the remaining cell capacity at the next and current time steps, respectively, while $Q_{capacity}$ is the nominal battery capacity. The constant current I is positive for charging and negative for discharging, with $I(t) = I(t+1) = I$. The relationship between capacity change and current is then derived as follows:

$$Q\,(t+1) - Q\,(t) = I\,\frac{\Delta t}{3600} \tag{2}$$

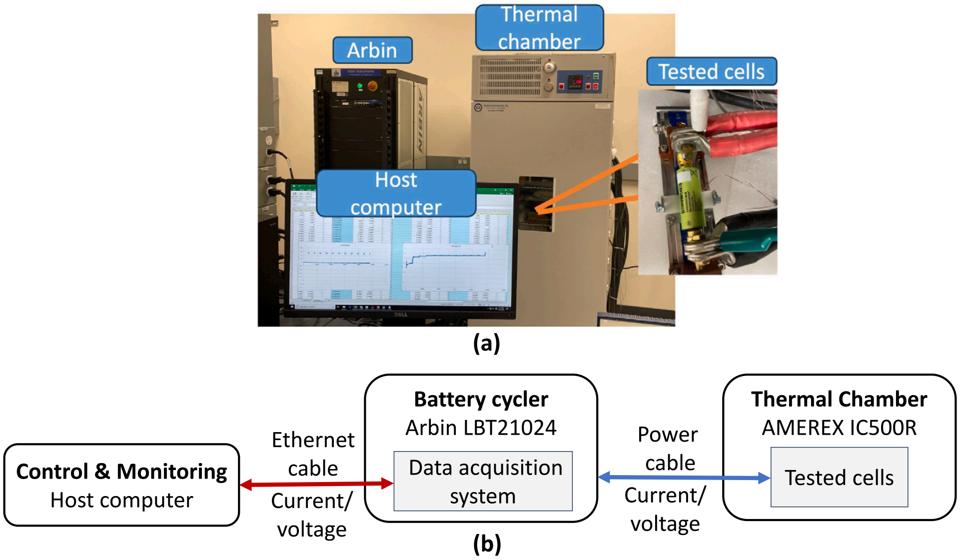

Fig. 2. Battery cell testing equipment at Stanford Energy Control Laboratory [34]. (a) battery cycler thermal chamber, tested cells, and host computer. (b) Functional block diagram showing key components and connections for control, data acquisition, and cell testing.

Table 2
SOC ranges for pulses at 1/30C(charge/discharge), 0.2C(charge/discharge) and 0.5C(charge).

Pulse number	1/30C Char.		1/30C Dis.		0.2C Char.		0.2C Dis.		0.5C Char.	
	SOC start	SOC end	SOC start	SOC end	SOC start	SOC end	SOC start	SOC end	SOC start	SOC end
a	0.16	0.17	0.17	0.15	0.00	0.05	0.13	0.03	0.00	0.05
b	0.33	0.34	0.34	0.32	0.05	0.10	0.22	0.13	0.05	0.10
c	0.50	0.51	0.51	0.49	0.10	0.20	0.32	0.22	0.10	0.19
d	0.67	0.68	0.68	0.66	0.20	0.30	0.42	0.32	0.19	0.29
e	0.84	0.86	0.85	0.83	0.30	0.40	0.51	0.42	0.29	0.38
f					0.40	0.50	0.61	0.51	0.38	0.48
g					0.50	0.60	0.71	0.61	0.48	0.57
h					0.60	0.70	0.81	0.71	0.57	0.67
i					0.70	0.80	0.90	0.81	0.67	0.76
j					0.80	0.90	0.95	0.90	0.76	0.86
k							1.00	0.95	0.86	0.95

Table 3
SOC ranges for pulses at 0.5C(discharge), 1C(charge/discharge) and 2C(charge/discharge).

Pulse number	0.5C Dis.		1C Char.		1C Dis.		2C Char.		2C Dis.	
	SOC start	SOC end	SOC start	SOC end	SOC start	SOC end	SOC start	SOC end	SOC start	SOC end
a	0.14	0.04	0.00	0.05	0.13	0.03	0.00	0.05	0.13	0.03
b	0.23	0.14	0.05	0.10	0.22	0.13	0.05	0.08	0.23	0.13
c	0.33	0.23	0.10	0.19	0.32	0.23	0.10	0.19	0.32	0.23
d	0.43	0.33	0.19	0.29	0.42	0.32	0.19	0.29	0.42	0.32
e	0.52	0.43	0.29	0.39	0.52	0.42	0.29	0.39	0.52	0.42
f	0.62	0.52	0.39	0.48	0.61	0.52	0.39	0.48	0.61	0.52
g	0.71	0.65	0.48	0.58	0.71	0.65	0.48	0.54	0.71	0.61
h	0.81	0.71	0.58	0.68	0.81	0.74	0.58	0.68	0.81	0.71
i	0.90	0.81	0.68	0.77	0.90	0.84	0.68	0.78	0.90	0.85
j	0.95	0.93	0.77	0.87	0.95	0.91	0.78	0.87	0.95	0.91
k	1.00	0.95	0.87	0.97	1.00	0.96	0.87	0.97	1.00	0.96

From Eq. (2), DQV is obtained as:

$$DQV(t) = \frac{Q(t+1) - Q(t)}{V(t+1) - V(t)} = \frac{I}{V(t+1) - V(t)} \frac{\Delta t}{3600} \tag{3}$$

where $V(t)$ is the cell voltage at time step t, and $V(t+1)$ is cell voltage at the next time step, $t+1$.

The complete DQV is calculated from raw current and voltage data using Eq. (3), shown as the green curve in Fig. 6b for a 0.5C discharge. Due to noise, this curve is not ideal for estimation tasks. To address this, the raw data is smoothed.[1] Since SOC changes monotonically during charging and discharging, DQV is a function of SOC, as shown in Fig. 6c. Final DQV curves at various C-rates (±1/30C, ±0.2C, ±0.5C, ±1C, and ±2C) are stored as 1-D lookup tables (Fig. 10), with SOC on the x-axis and DQV values on the y-axis. These are referred to as $\mathrm{DQV}_{complete}$.

---

[1] The raw data was smoothed using MATLAB's *smoothdata* function.

(a) Charge voltage vs. SOC

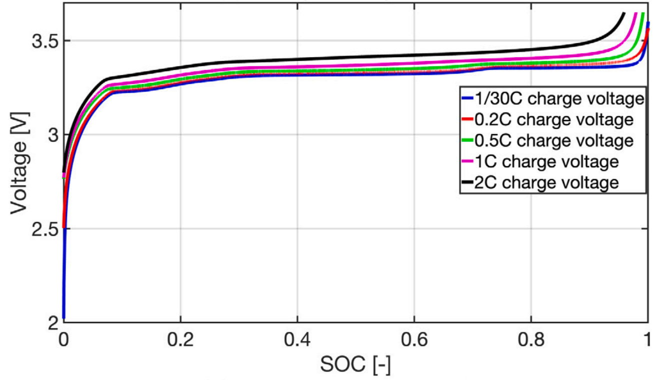

(b) Discharge voltage vs. SOC

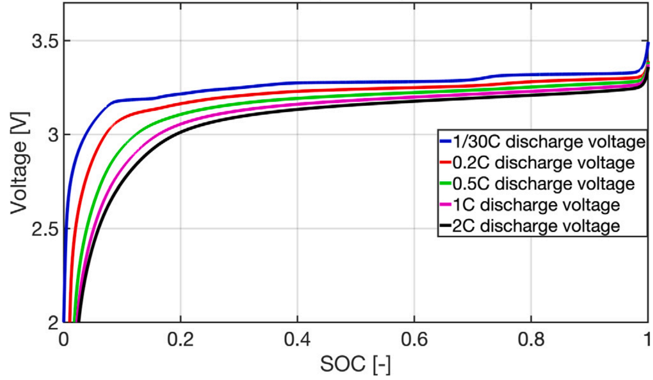

Fig. 3. Experimental voltage curves plotted against SOC for constant current charge (a) at rates of 1/30C, 0.2C, 0.5C, 1C, and 2C, and constant current discharge (b) at the same rates (25 °C).

3.2. Algorithm part B: Pulse DQV curve generation

SOC estimation is performed using the applied current pulse and the corresponding voltage response, as shown in Fig. 7. To mitigate the effects of measurement noise, a data filtering process is applied prior to DQV calculation. The details of this filtering process are outlined in Section 3.4. After filtering the voltage data, the pulse DQV values are computed using Eq. (3), as shown in Fig. 7.

3.3. Algorithm part C: DQV-based SOC estimation algorithm

The algorithm is illustrated in Fig. 8. The DQV-based model for SOC estimation is based on the following equations [35]:

$$SOC(t) = SOC(t-1) + I\frac{\Delta t}{Q_{\text{capacity}}} \tag{4}$$

$$y = DQV_{complete}(SOC) \tag{5}$$

where $SOC\,(t)$ and $SOC\,(t-1)$ are SOC at present time step t and previous time step $t-1$, respectively, $Q_{capacity}$ is the cell nominal capacity. Finally, $DQV_{complete}(SOC)$ is the pre-processed 1D look-up table that returns the DQV value (i.e., computed output y) as a function of SOC, as shown in Fig. 6.[2] The model-based SOC observer built on Eqs. (4)–(5) is given by:

$$\widehat{SOC}(t) = \widehat{SOC}(t-1) + I\frac{\Delta t}{Q_{capacity}} + G(y - \hat{y}) \tag{6}$$

$$\hat{y} = DQV_{pulse}(\widehat{SOC}) \tag{7}$$

where G is the observer gain, and the DQV_{pulse} is the DQV built upon current pulses given to the battery at unknown (to be estimated) SOC values. The observer gain, G is designed using an UKF. The UKF structure offers robustness to modeling uncertainties and input noise, making it suitable for real-time on-board implementation [19]. The detailed UKF calculation is presented in Table 4 (Appendix).

In this study, complete DQV curves, $DQV_{complete}$ are collected at various C-rates (i.e., ±1/30C, ±0.2C, ±0.5C, ±1C, and ±2C), and stored as DQV-SOC look-up tables. The new observer scheme proposed here circumvents the challenges in observer design for LFP, where the flat OCV curve leads to poor observability, making SOC estimation via OCV inversion unreliable [22]. In contrast, by leveraging the DQV curve, SOC can be uniquely determined due to the presence of distinct valleys and peaks, enhancing observability. During a pulse of length N samples (1 Hz in this study), the UKF performs N sequential measurement updates with Steps 9–12 in Table 4. Because these updates span the entire pulse window, the estimator effectively matches the shape of the measured pulse DQV segment to the reference complete DQV curve in the lookup table, rather than relying on any single instantaneous value. This segment-wise approach enables the estimator to resolve SOC values even in regions where the overall DQV–SOC relationship is locally non-monotonic.For more detailed information on the UKF calculation process, please refer to [36,37].

3.4. Experimental pulse data filtering and DQV calculation

The pulse discharge and charge voltage are the basis for the calculation of DQV_{pulse}. The raw experimental data contains noise that must be filtered to obtain a smooth DQV curve. The lower the current rate, the lower the signal-to-noise ratio (SNR). Fig. 9a shows the noisy voltage data from a 1/30C discharge over 1800 s (pulse e), sampled at 1 Hz. The noisy data makes it challenging to extract useful features from the DQV curve.

Moving-average filtering is a widely-used method for smoothing signals [38]. The moving average filter is calculated as [38]:

$$F\,(r) = \frac{1}{M}\sum_{J=0}^{M-1} x_s(r+J) \tag{8}$$

where x_s is the input signal, F is the filtered output signal, and M is the smoothing window size. In this paper, we use a Gaussian-weighted average filter for comparison.[3]

Fig. 9a presents the raw voltage and current data of a 1/30C discharge pulse (pulse e in Fig. 4a). The window size of the averaging filter serves as a crucial tuning parameter in achieving a smooth signal. Fig. 9b compares Gaussian-weighted filters with window sizes of 1 and 10, demonstrating that larger window sizes result in progressively smoother voltage curves.

Although the filtered voltage curves retain the general shape of the raw data, significant noise remains, making them unsuitable for further DQV calculations. Fig. 9c illustrates that the DQV curves obtained from the moving-average filter with window sizes of 1 and 10 are distorted, obscuring critical features such as peak positions, making it challenging to extract meaningful insights. Hence, increasing the window size (>10) is conductive to larger errors.

To address this issue, we propose a mathematical model to fit the voltage behavior (V_t) when discharge/charge pulse currents are applied. The model uses two exponential terms, as shown in the following equation:

$$V_t = p_1 e^{p_2 t} + p_3 e^{p_4 t} + V_0 \tag{9}$$

---

[2] The Matlab $interp1$ function interpolates between two neighboring data points to estimate the value y at a specific SOC query point in the 1-D map $DQV_{complete}(SOC)$.

[3] In Matlab, the Gaussian-weighted average filter is implemented using the $smoothdata$ function.

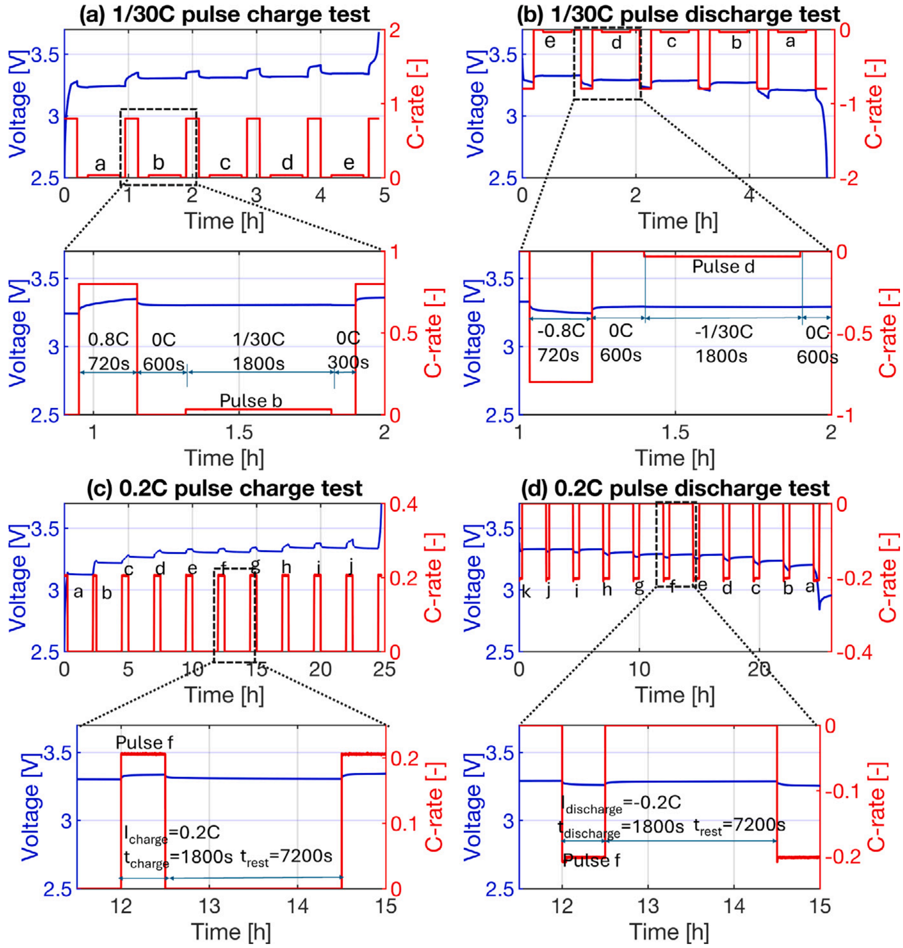

Fig. 4. Experimental current and voltage data for charge and discharge pulse tests at rates of 1/30C and 0.2C. (a) 1/30C charge pulses; (b) 1/30C discharge pulses; (c) 0.2C charge pulses; (d) 0.2C discharge pulses (25 °C).

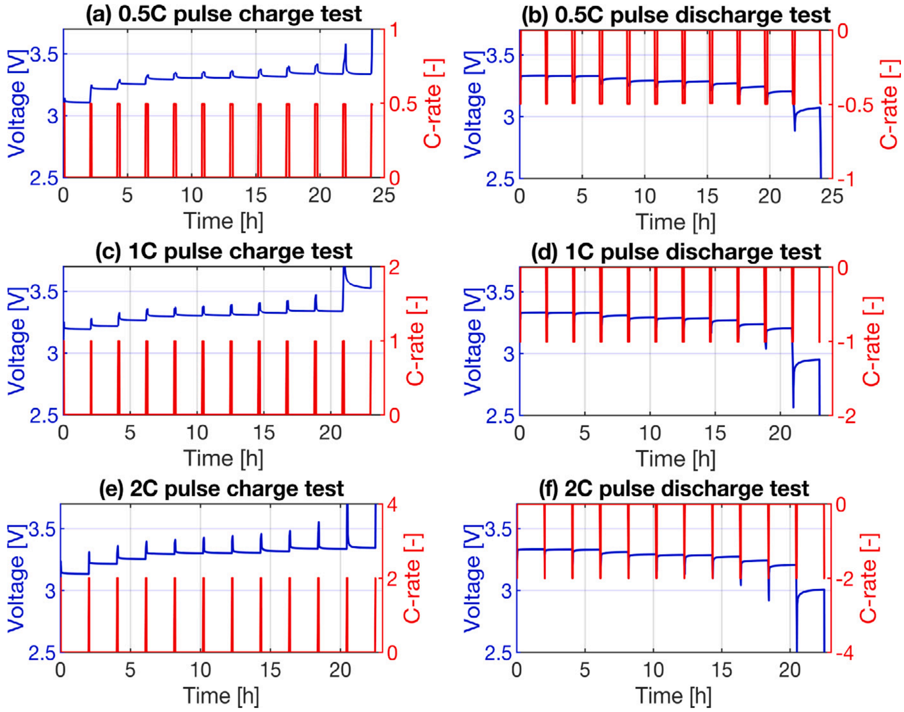

Fig. 5. Experimental current and voltage data for charge and discharge pulse tests at different C-rates: (a) 0.5C charge pulse; (b) 0.5C discharge pulse; (c) 1C charge pulse; (d) 1C discharge pulse; (e) 2C charge pulse; (f) 2C discharge pulse. (25 °C).

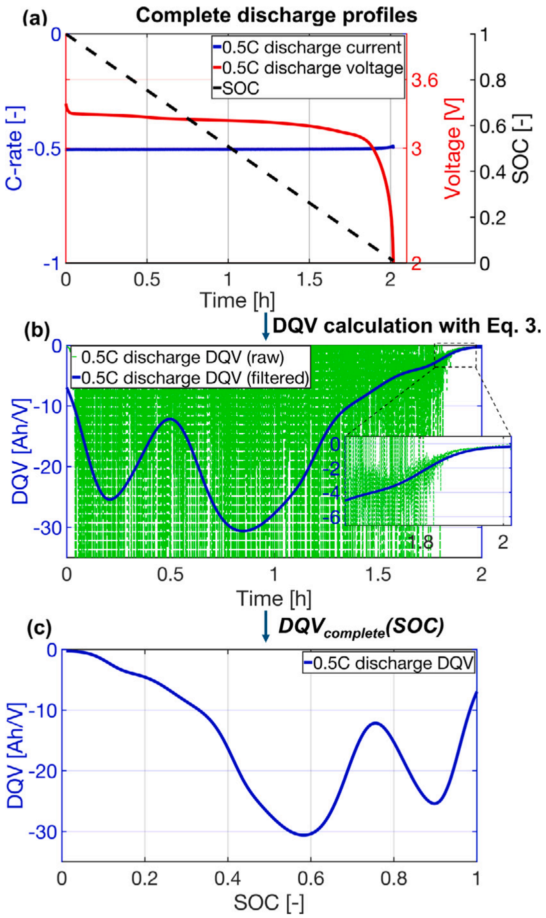

Fig. 6. Calculation of complete DQV curve using 0.5C discharge current: (a) 0.5C discharge current, voltage and SOC vs. time; (b) 0.5C discharge complete DQV vs. time: raw data and filtered data. (c) complete DQV vs. SOC with filtered data, which we refer to as $DQV_{complete}(SOC)$.

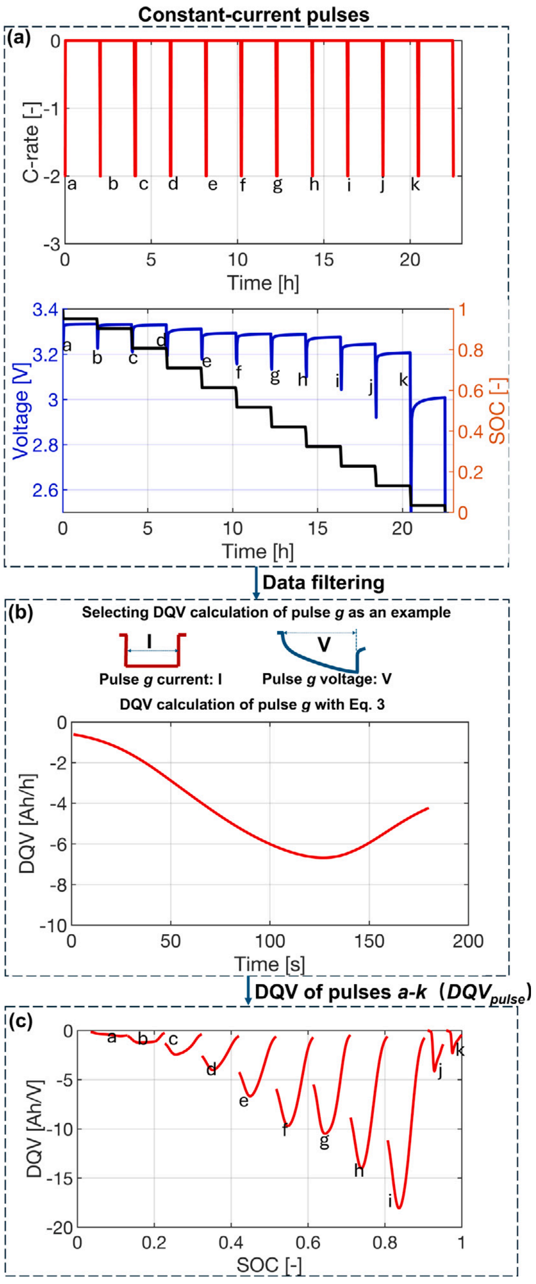

Fig. 7. Calculation of pulse DQV curves using 2C discharge current pulses: (a) 2C discharge current pulses and corresponding voltage and SOC profiles; (b) Pulse DQV at 2C discharge. (c) DQV calculated over current pulses as a function of SOC.

where p_1, p_2, p_3, and p_4 are parameters obtained through curve fitting, t is time and V_0 is the initial voltage value when the pulse current is applied. The curve fitting process minimizes the error between the simulated voltage (using Eq. (9)) and the experimental voltage V_{exp} :

$$minimize \sum_{t=1}^{N} \left(V_{exp}[t] - V_t[t]\right)^2 / N \tag{10}$$

where N is the number of data points.[4]

As depicted in Fig. 9b, the voltage obtained through the exponential fitting with the 1/30C discharge current exhibits smoother behavior compared to the moving average filtered data . The RMSE of the filtered voltage is 0.185 mV. Finally, the resulting DQV curve obtained using the exponential fitting voltage is shown in Fig. 9c. In this paper, the exponential fitting method is used for processing raw voltage data before DQV calculations with pulse currents. Unlike the moving average filter, the exponential filter eliminates the need for window size adjustments. This method effectively reduces noise and distortion in the voltage signal, producing accurate and reliable DQV curves that are suitable for state estimation purposes. Fig. 10 compares the DQV curves obtained from the pulse charge/discharge data (±1/30C, ±0.2C, ±0.5C, ±1C, and ±2C) shown in Figs. 4–5. The current pulses with the same C-rate are denoted by $a-k$ corresponding to SOC from low to high. The initial and final SOC for each pulse at different C-rates are summarized in Tables 2–3. For comparison, the complete DQV curves with constant currents (±1/30C, ±0.2C, ±0.5C, ±1C, and ±2C) are also plotted in Fig. 10.

In Fig. 10a, the DQV curves of 1/30C pulse currents for 1800 s are difficult to align with the complete 1/30C DQV curve, indicating that the duration of pulse current with 1/30C should be extended. As the C-rate increases to 0.2C (1800 s), more DQV crossings are found in Fig. 10b. A similar trend can be seen in Fig. 10c with 0.5C (720 s). However, when applying 1C (360 s) and 2C (180 s) pulses, the pulse DQV curves with pulse currents deviate from the complete DQV curves, as depicted in Fig. 10d and Fig. 10e, respectively. This deviation is likely caused by transient polarization effects dominating the voltage response immediately after the pulse current is applied, especially following a long rest period. In contrast, the complete DQV

---

[4] The fitting process is calculated with the fit function in Matlab.

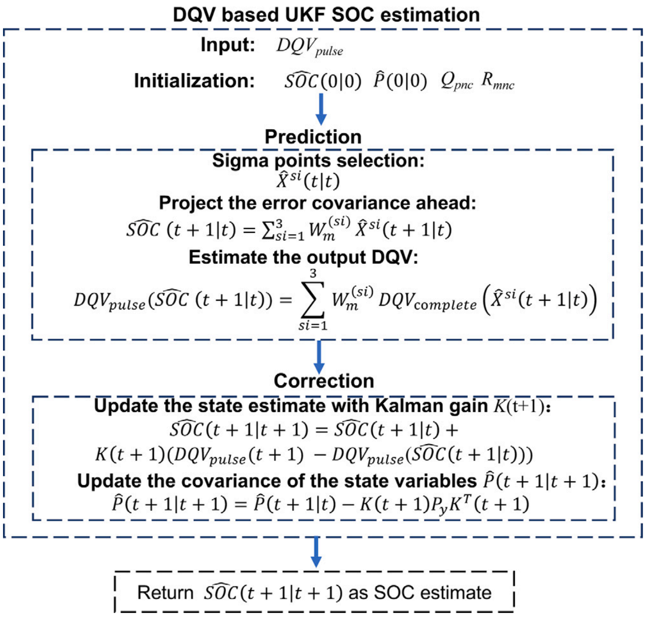

Fig. 8. DQV-based SOC estimation using UKF. This process includes initialization, prediction, and correction steps, as well as sigma point selection (where si is the order of sigma points), error covariance projection, and Kalman gain update. The detailed UKF implementation process is described in Table 4.

curves are obtained under quasi-steady-state conditions with stabilized polarization, leading to higher DQV values.

4. SOC estimation results and discussion

For illustration, SOC estimation is demonstrated using 0.5C discharge pulses. The corresponding current profiles serve as inputs to the estimator. Raw voltage data are smoothed via exponential fitting, and the resulting DQV curves are used in the UKF. The initial SOC is offset by 0.1, and convergence is defined as the estimation error falling within ±0.02.

Five 0.5C discharge pulses, arranged from low to high SOC ranges, are labeled as *a, b, c, d*, and *e*, respectively, as shown in Fig. 11a. The exact SOC ranges for these current pulses (*a-e*) are listed in Table 3. As shown in Fig. 11a, each pulse DQV corresponds to a specific SOC range. Within this SOC range, the pulse DQV represents a segment of the complete DQV curve, which is denoted as Sa, Sb, Sc, Sd, and Se for pulses *a*, *b*, *c*, *d*, and *e*, respectively. These corresponding segments are illustrated in Fig. 11a.

In certain SOC regions, the pulse-DQV segment overlaps with the corresponding portion of the complete DQV curve and is locally monotonic, which greatly supports the UKF correction step. By leveraging this overlap, the segment-wise approach enables the estimator to determine SOC accurately even when the overall DQV–SOC relationship is locally non-monotonic. In practice, the SOC estimation error is corrected by the UKF based on the discrepancy between the estimated output $\hat{y}$ and measured output y. Consequently, the effectiveness of the correction step depends strongly on the degree of alignment between the measured pulse-DQV segment and the corresponding section of the complete DQV profile.

Specifically, the overlap between Sa–Se in the complete DQV and the pulse *a*–*e* DQV directly influences the estimation accuracy. In Fig. 11a, the DQV of pulse *a* closely aligns with Sa in the complete DQV, with the overlapping region highlighted in gray. Pulse *b* partially overlaps with segment Sb of the complete DQV, though less than pulse *a*. Similarly, pulse *c* exhibits some alignment but the overlap is smaller compared to *a* and *b*. In contrast, pulses *d* and *e* show no overlap with the complete DQV, with pulse *e* being the farthest. This is mainly due to the higher absolute DQV values in that SOC range, making it difficult for short pulses to align unless their duration is extended. Based on the degree of alignment, SOC estimation is most accurate with pulse *a*, followed by *b* and *c*, while *d* and *e* yield the least accurate results. This confirms that the estimator exploits pulse-level information instead of a single DQV sample, which is crucial in non-monotonic regions.

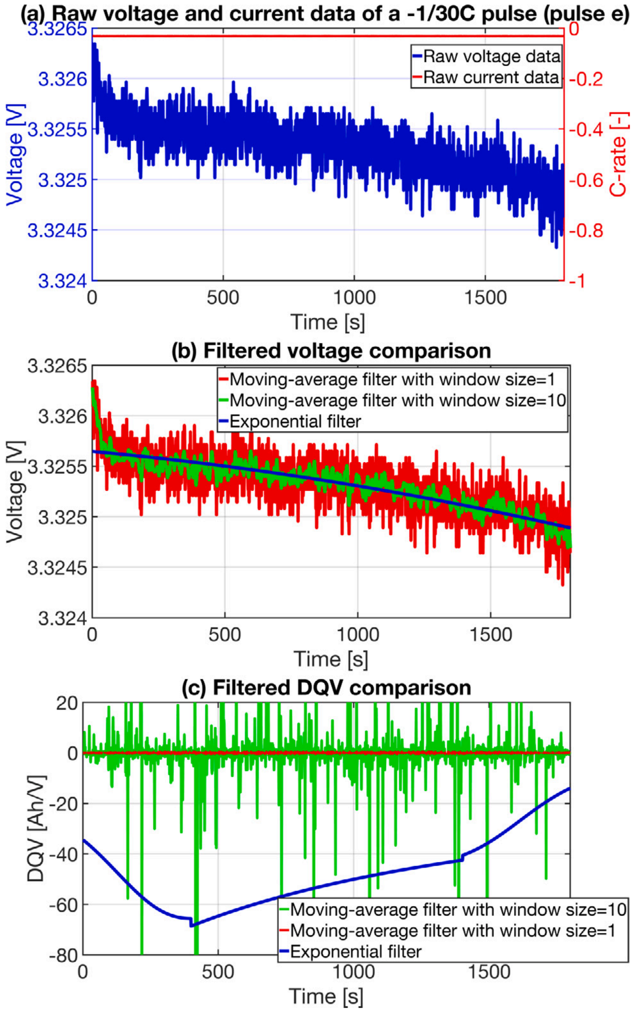

Fig. 9. (a) Raw voltage and current profiles of a −1/30 pulse (pulse *e* in Fig. 4a, the SOC range of this pulse is [0.83, 0.85]); (b) filtered voltage curves using different window sizes for the moving-average filter, along with the exponential filtered voltage; (c) filtered DQV curves for different window sizes of the moving-average filter and the exponential filtered DQV.

The SOC root mean square error (RMSE) is defined as:

$$SOCRMSE = \sqrt{\frac{1}{N}\sum_{t=1}^{N}\left(\widehat{SOC}(t) - SOC_{reference}(t)\right)^2} \tag{11}$$

where $SOCRMSE \in [0,1]$, N is the number of SOC estimation ($\widehat{SOC}$) points, $SOC_{reference}$ is the reference SOC from Coulomb counting.

The SOC estimation errors for the 0.5C discharge pulse profiles (*a*–*e*) are shown in Fig. 11b. For pulse *a*, the SOC estimation error decreases to 0.01 within 180 s. For pulse *b*, the SOC estimation error is reduced to 0.01 after 540 s. Similarly, for pulse *c*, the SOC estimation converges successfully after 493 s. However, for pulses *d* and *e*, SOC estimations fail to converge due to minimal or no overlap with the complete DQV curve at 0.5C. The SOC root mean square errors (RMSEs) for pulses *a-e* are 0.0256, 0.079, 0.1246, 0.1738, and 0.1960, respectively. Notably,

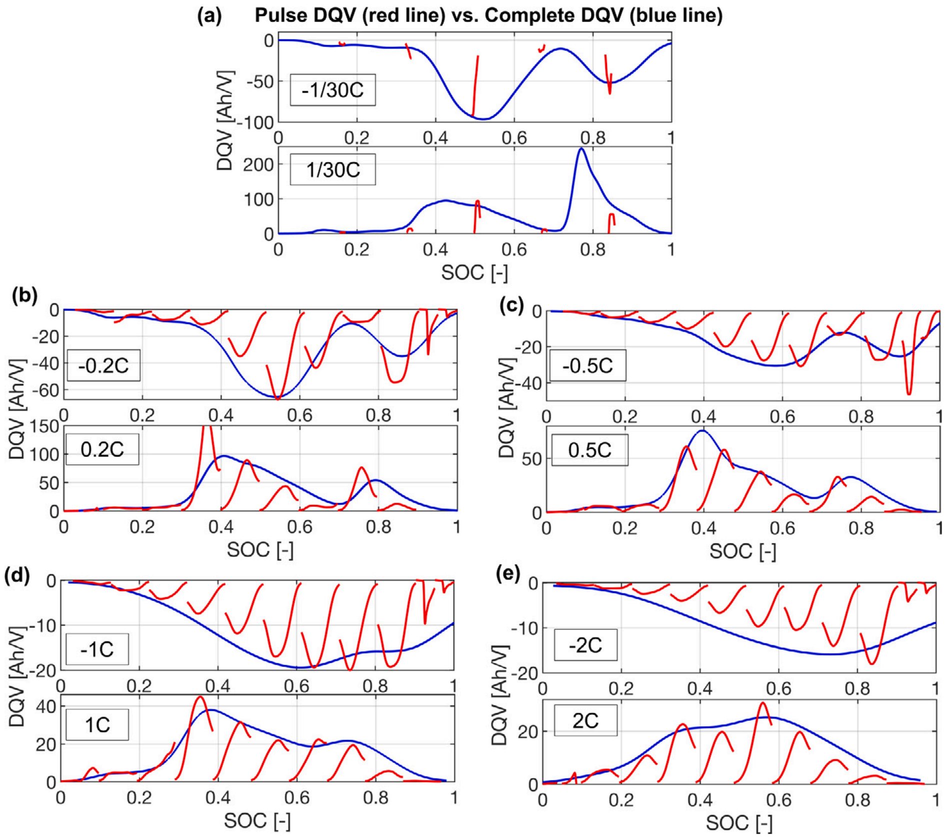

Fig. 10. Obtained pulse DQV with filtered pulse current data compared with complete DQV curves at ±1/30C (a), ±0.2C (b), ±0.5C (c), ±1C (d), ±2C (e).

pulse *a* exhibits the lowest RMSEs for SOC estimation, followed by pulses *b* through *e*. We now analyze SOC estimation performance using current pulses at different C-rates (1/30C, 0.2C, 0.5C, 1C, and 2C). Fig. 12 illustrates the SOC RMSE after convergence for each C-rate, with subfigures (a) through (e) corresponding to 1/30C through 2C, respectively. Fig. 12a (1/30C) shows that only three pulses yield convergent SOC estimation in the SOC range of 0.3–0.7. The low current 3600 s pulse allows full voltage settling, yielding pulse DQV curves that align well with the reference. However, SOC estimation fails to converge at low and high SOC, likely due to weak excitation or low signal-to-noise ratio. Fig. 12b (0.2C) reveals reduced RMSE in the low SOC region (0–0.3) compared to 1/30C. Nevertheless, estimation fails in the mid-SOC region (0.4–0.5). Fig. 12c (0.5C) exhibits additional convergence failures in the mid-to-high SOC range (0.5–0.7). As the C-rate increases, voltage responses become more distorted due to polarization and resistive effects, making the extracted pulse DQV less representative of the complete DQV. In these SOC regions, where the OCV curve is also relatively flat, dynamic distortion further impairs the observability of the state, challenging the estimator's correction step. In Fig. 12d and e for the 1C and 2C case, estimation performance degrades significantly in the 0.4–1.0 SOC range. At higher C-rates, transient polarization effects induce larger instantaneous voltage changes, resulting in lower pulse DQV and reduced alignment with the complete DQV, leading to SOC estimator failure. Although higher C-rates improve the SNR, they can distort the pulse DQV, causing it to deviate from the complete DQV and reducing the effectiveness of the UKF's correction step. In conclusion, moderate pulse currents (e.g., 0.2C to 0.5C) offer the best trade-off: large enough to generate pulse DQV while avoiding significant distortion or misalignment. The SOC estimation framework thus performs most reliably when pulse amplitudes are sufficiently informative yet remain consistent with the reference DQV model. For practical deployment, a C-rate-adaptive pulse strategy may be required to ensure robust SOC estimation across all regions.

4.1. Filter selection on SOC estimation

To further investigate the impact of filter selection on DQV-based SOC estimation, we applied the same 1C discharge pulse for 360 s (as described in Section 2) as input to the SOC estimator, with different filters applied to the pulse signal. Specifically, we compared the exponential filter and the moving-average filter with window sizes of 10 and 100. A detailed description of these filters is provided in Section 3.2 and Fig. 9.

Fig. 13 presents the SOC estimation results and errors obtained using different filters applied to the DQV-based pulse input. The exponential filter (red) and moving-average filters with window sizes of 10 (cyan) and 100 (black) are compared to evaluate their impact on SOC estimation accuracy. In Fig. 13a, the SOC estimation results indicate that while all filters generally follow the reference SOC (magenta), the moving-average filter with a large window size (100) and exponential filter smooth fluctuations. Fig. 13b further quantifies SOC estimation errors, showing that while the exponential filter and larger window size (100) moving-average filter can maintain lower errors, the smaller window size (10) results in a more pronounced deviation.

In summary, we evaluated both Gaussian-weighted moving-average filters (with various window sizes) and an exponential filter for smoothing pulse voltage measurements. The results highlight the advantage of the exponential filter in maintaining accuracy while effectively reducing noise and fluctuations, making it a superior choice for SOC estimation compared to moving-average filters with small window sizes. Therefore, exponential fitting was adopted as the default filtering method throughout this study. This smoothing approach is robust to high-frequency noise and produces smooth, physically plausible voltage profiles from which DQV is derived. Regarding the voltage measurement accuracy, voltage resolution of 1 mV or better is recommended and current measurement should have consistent time resolution and minimal drift.

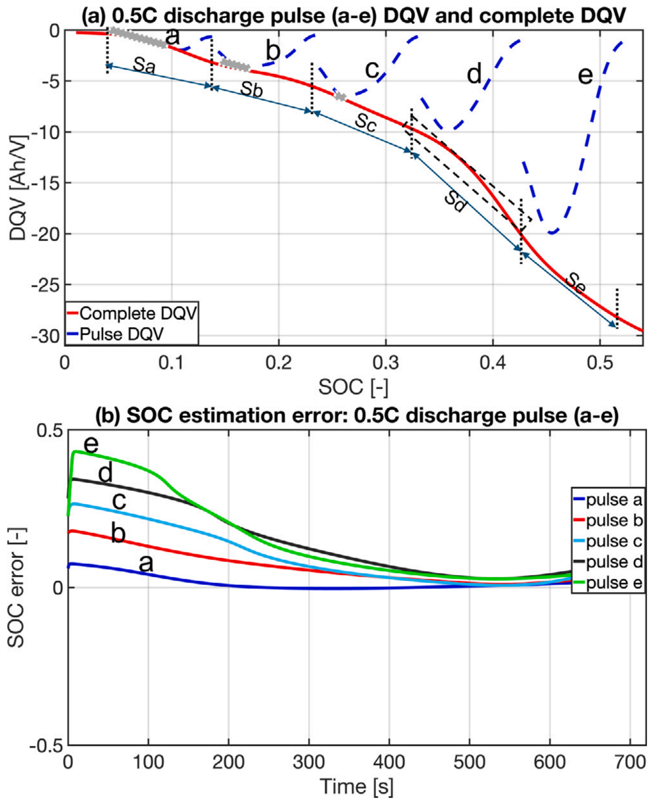

Fig. 11. (a) Comparison between DQV curves derived from 0.5C discharge pulses (a–e) and the complete 0.5C discharge DQV curve. The gray regions highlight the overlap between pulse-derived and reference DQV segments, which strongly influence estimation accuracy. The 0.5C C-rate is selected as it offers a favorable trade-off between SNR and polarization distortion: higher than 0.2C for better SNR, yet moderate enough to avoid the significant transient effects seen at 1C or 2C. (b) SOC estimation errors corresponding to panel (a).

4.2. The impact of temperature on DQV vs. SOC

Fig. 14 compares the DQV profiles of 0.5C discharge at two different temperatures, 25 °C (red curve) and 45 °C (blue curve), as a function of SOC. The DQV profiles exhibit notable differences influenced by temperature, particularly in the intermediate SOC range. At 45 °C, the DQV curve shows sharper peaks and steeper gradients in the SOC range of approximately 0.4–0.8. These pronounced features result from improved reaction kinetics and lower internal resistance at elevated temperatures, which enhance the battery's ability to transfer charge during discharge. The sharper transitions in the DQV curve at 45 °C indicate more significant voltage changes for the same charge transfer, highlighting the impact of temperature on the battery's voltage response. Conversely, at 25 °C, the DQV curve displays smoother transitions and lower peak values in the same SOC range. This behavior reflects slower reaction kinetics and higher polarization effects at lower temperatures, which dampen the changes in the DQV profile. This finding demonstrates how temperature significantly affects the DQV vs. SOC relationship, particularly in the mid-SOC range, underscoring the importance of accounting for temperature in SOC estimation algorithms.

4.3. Comparison with Voltage-SOC curve based method

We selected pulse *b* from the 2C discharge experiment as a representative case and applied both methods under identical conditions. For the Voltage–SOC curve method, a full discharge was performed at 2C (the same C-rate as the tested pulse). The true SOC was calculated by integrating current over time using Coulomb counting, while terminal voltage was recorded continuously. This produced a monotonic Voltage–SOC profile, which was stored as a lookup table for inverse interpolation. During the 2C pulse test, the filtered voltage curve was mapped to SOC using linear interpolation on the inverse Voltage–SOC curve, yielding a single-point SOC estimate. For the DQV-based method, the same filtered voltage signal during the pulse was used to compute the DQV segment, and the SOC was estimated as illustrated in Fig. 8. As shown in Fig. 15a, the DQV-based method tracks the true SOC more accurately and converges faster than the Voltage–SOC approach. The Voltage–SOC estimate shows an offset and lags behind the true SOC. Fig. 15b quantifies the error over time, demonstrating that the DQV-based method maintains lower estimation errors throughout the pulse window, whereas the Voltage–SOC method yields larger errors. These results confirm the advantages of the DQV-UKF approach in both accuracy and convergence.

4.4. Limitations and mitigation strategies

As shown in the results (e.g., Fig. 12d–e), convergence failures of the proposed DQV-based SOC estimation framework predominantly occur for high C-rates (e.g., 1C and 2C) at mid-to-high SOC ranges (e.g., 0.5–0.9). First, at high C-rates, the voltage response exhibits significant resistive and capacitive transients, leading to dynamic polarization effects. These distortions affect the extracted pulse DQV segments, making them differ from the steady-state reference DQV curves. This can reduce the reliability of the UKF's innovation term, lowering estimation accuracy and sometimes causing divergence. Second, in the 0.5–0.9 SOC range, convergence issues mainly stem from insufficient overlap between the pulse-derived DQV segment and the corresponding section of the complete DQV reference curve. This happens because the short pulse does not cause enough SOC change or voltage variation to capture the key features of the full DQV curve in this region. As a result, the innovation term calculated by the UKF becomes less informative or even misleading, especially when combined with distortions from high C-rate pulses. These findings highlight a key trade-off in pulse design: higher C-rates improve signal-to-noise ratio and speed up SOC changes but can introduce polarization effects that distort the DQV shape. Conversely, lower C-rates reduce polarization distortion but may generate DQV segments that are too narrow or flat to align well with the reference. Managing this balance carefully is essential for maintaining reliable SOC estimation across the entire SOC range.

To address these limitations and improve estimation performance, we propose strategies focused on pulse design, algorithm robustness, and reference modeling. Optimizing pulse design involves adjusting pulse duration and C-rate to better approximate quasi-steady-state conditions, such as using longer pulses in the 0.5–0.9 SOC range and incorporating short pre-pulse rest intervals at high C-rates to reduce transient effects. Applying pseudo-continuous sequences of short pulses with minimal rest would help balance polarization reduction and temporal resolution. On the algorithmic side, integrating polarization relaxation models and advanced filtering techniques like exponential fitting could help correct transient voltage deviations, enhancing the UKF's robustness. Additionally, adapting the UKF's measurement noise covariance based on C-rate and SOC region could improve estimation. Finally, in SOC regions where pulse-derived DQV segments are less reliable, a hybrid estimation approach can temporarily rely on Coulomb counting or voltage-model predictions, switching back to DQV-based corrections when sufficient pulse information is available. Together, these strategies aim to enhance convergence and broaden the applicability of the DQV-UKF framework across a range of C-rates and real-world deployment conditions.

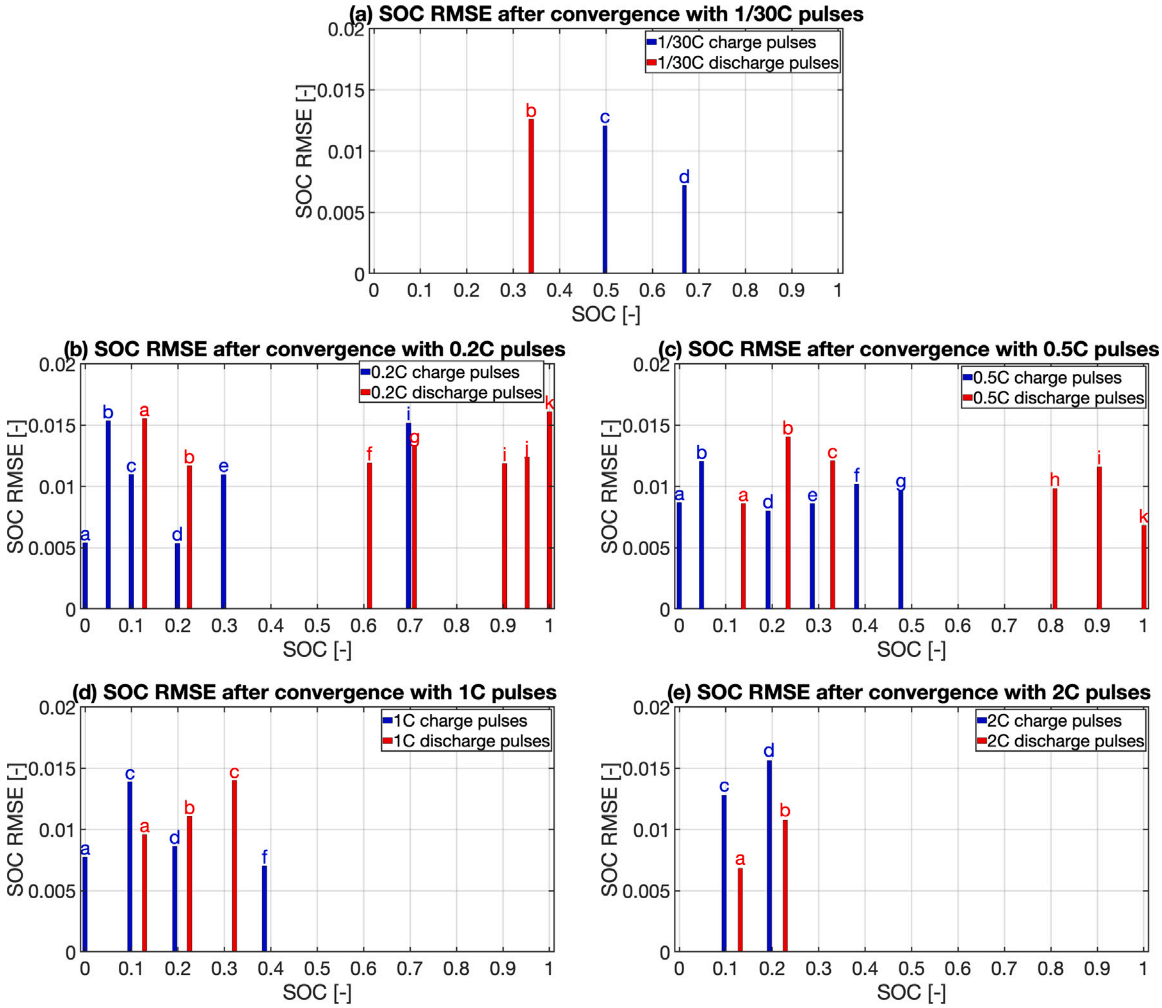

Fig. 12. SOC estimation RMSEs after convergence under different pulses: 1/30C (a), 0.2C (b), 0.5C (c), 1C (d), and 2C (e). Each subplot includes only the pulses that result in convergent SOC estimation. Labels a, b, c, etc., correspond to individual pulses. Red bars represent discharge pulses, while blue bars indicate charge pulses. The x-axis position of each bar reflects the initial SOC at which the corresponding pulse was applied.

4.5. Comparative advantages and real-world applicability

Compared with data-driven approaches, physics-based models (e.g., P2D, SPM), ECM, and hybrid model-fusion techniques, the proposed DQV-based SOC estimation framework offers a practical balance of ease of deployment, low calibration effort, and low computational requirements, making it especially well suited for LFP batteries. The practical advantages of the proposed DQV-based SOC estimation framework are as follows. First, it enhances SOC observability in LFP cells by transforming the typically flat voltage–SOC relationship into a SOC-sensitive DQV curve. This transformation allows the model-based SOC estimation problem to be reformulated using the calculated output (DQV) instead of the measured output (OCV), improving estimation accuracy—especially in mid-SOC regions where traditional OCV- or ECM-based estimators often struggle due to limited voltage resolution. Unlike physics-based models that require detailed electrochemical parameters or deep learning methods that depend on large labeled datasets, this approach relies on experimentally obtained DQV–SOC lookup tables. The core estimator is a lightweight one-dimensional UKF that uses only three sigma points and simple scalar operations. Since estimation is triggered intermittently — such as by a current pulse — rather than continuously, the average computational load remains low. This makes the method well suited for implementation on BMSs with limited processing power and memory resources.

Although this work is partly motivated by the growing use of LFP batteries in EVs, the framework is not limited to automotive applications. It is also well suited for stationary grid-connected battery systems. In these grid applications, short diagnostic pulses can be applied opportunistically—during periods of low demand or maintenance—to trigger a DQV-based correction. This approach periodically calibrates the SOC estimate, compensating for drift in Coulomb counting or ECM-based methods without the need for continuous monitoring.

For reference, a standard UKF implementation with a second-order ECM for SOC estimation typically estimates three states (SOC and two RC-pair voltages), requiring the propagation of 2*3+1 = 7 sigma points per iteration and repeated evaluation of the ECM equations [8]. In contrast, our proposed framework estimates only a single state (SOC), reducing the UKF to 2*1+1 = 3 sigma points per iteration. The model output is obtained directly from a preloaded one-dimensional DQV–SOC lookup table via interpolation, without solving differential equations or computing ECM parameters. Therefore, it can be reasonably inferred that this streamlined state dimension and simple measurement model significantly reduce the number of arithmetic operations, memory usage, and code complexity, making the method highly suitable for deployment on embedded BMS hardware with limited processing resources.

In summary, the proposed method is broadly applicable to both stationary and mobile battery systems, offering a practical, accurate,

(a) SOC estimation results with different filters

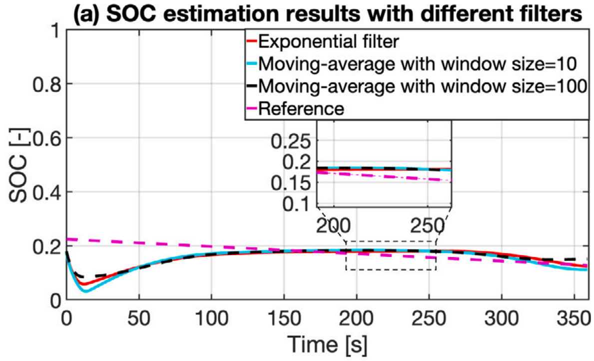

(b) SOC estimation errors with different filters

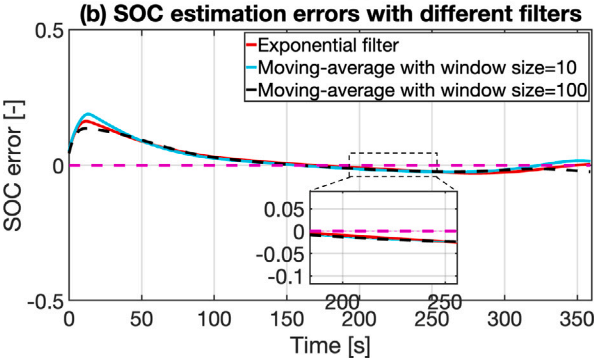

Fig. 13. Pulse *b* at 1C discharge with the SOC range of [0.13, 0.22] is selected as input for this SOC estimation. SOC estimation results (a) and errors (b) with different filters (Exponential filter (red), Moving-average filter with window size = 10 (cyan), and Moving-average filter with window size = 100 (black)). The referenced SOC is calculated with Coulomb counting (magenta).

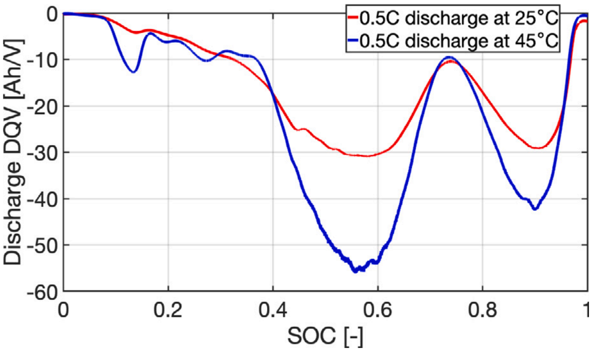

Fig. 14. DQV curves with 0.5C discharge at 25 °C and 45 °C.

and low-cost solution for SOC estimation with low computational, calibration, and maintenance requirements—especially where conventional techniques are limited by voltage flatness, model complexity, or system constraints.

(a) SOC estimation comparison with Voltage-SOC curve based method

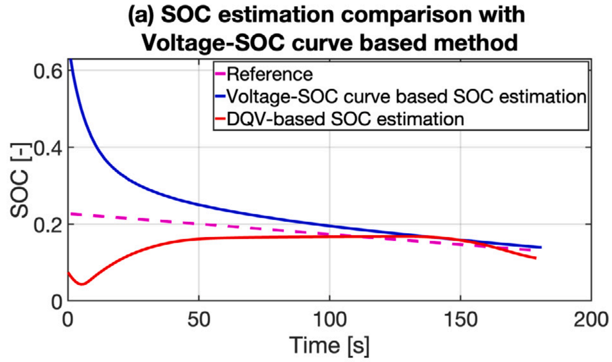

(b) SOC estimation errors

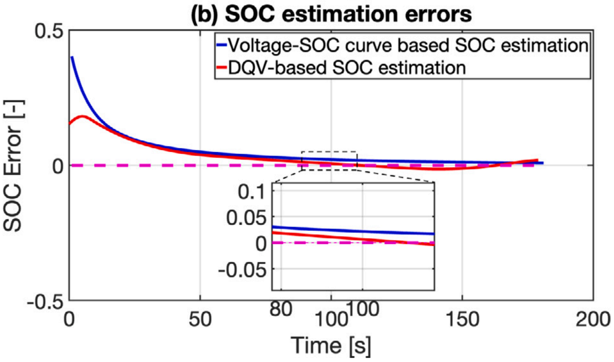

Fig. 15. Comparison of SOC estimation between OCV–SOC and DQV–SOC methods. Pulse *b* from the 2C discharge experiment, within the SOC range [0.13, 0.23], is selected as the input for comparison. Panel (a) shows the SOC estimates using the Voltage–SOC curve method (blue) and the DQV-based method (red), with the reference SOC obtained via Coulomb counting (magenta). Panel (b) shows the corresponding estimation errors for both methods.

5. Conclusion

This study introduces a novel DQV-based SOC estimation framework for LFP batteries, addressing the fundamental challenge of poor SOC observability caused by the flat OCV–SOC relationship. By recognizing the univocal mapping between SOC and DQV, we construct a model-based observer in which DQV curves — generated from short-duration current pulses — serve as the output measurement within a state-space estimation framework. Voltage responses are preprocessed using exponential fitting to suppress noise and transient artifacts, enabling the extraction of smooth pulse-DQV features that are processed through a UKF.

Key Findings: Experimental results show that C-rate pulses between 0.2C and 0.5C achieve an optimal balance between signal strength and polarization distortion, resulting in SOC estimation RMSEs below 0.08 with convergence times ranging from 180 to 540 s. For example, under a 0.5C pulse, the method achieves an RMSE of 0.0256. This approach avoids complex battery modeling and is well suited for real-time deployment on resource-constrained BMS platforms.

Limitations: Convergence failures were observed at high C-rates (1C and 2C) and in mid-to-high SOC regions (e.g., 0.5–0.9), primarily due to transient polarization effects and pulse-complete DQV misalignment. Furthermore, DQV profiles are sensitive to temperature variations particularly in regions where the voltage plateau dominates.

Future work will focus on enhancing the robustness, generalizability, and deployability of the proposed framework. This includes: (1) developing temperature-adaptive and aging-aware DQV reference tables; (2) exploring C-rate and SOC-region adaptive pulse design and pseudo-continuous excitation schemes to ensure reliable DQV curve matching and improve SOC estimation accuracy under dynamic operating conditions; (3) implementing advanced signal modeling techniques to correct for polarization transients; (4) conducting statistical assessments of DQV repeatability across multiple cells with varying geometries, chemistries, and cycle life stages to support scalable reference generation. We also plan to evaluate the real-time performance of the algorithm via hardware-in-the-loop testing and optimize its implementation on embedded BMS hardware, including low-power automotive-grade processors.

Table 4
UKF calculation process.

Step	Description
1	**Input:** $\widehat{SOC}(0\vert 0)$, $\widehat{P}(0\vert 0)$, $Q_{pnc,1\times 1}$, $R_{mnc,1\times 1}$
2	**Output:** $\widehat{SOC}(t+1\vert t+1)$, $\widehat{P}(t+1\vert t+1)$
3	**Require:** Initialization of state and error covariance matrix.
4	**State estimate at time step 0:** where $\widehat{SOC}(0\vert 0)$ represents the initial estimated states. The state estimation error covariance matrix at time step 0 is $\widehat{P}(0\vert 0)$. Q_{pnc} is the process noise covariance and R_{mnc} is the measurement noise covariance.
5	**For each time step** $t = 1, 2, \dots,$ **do**
6	**Choose the sigma points** $X^{si}(t\vert t)$: $X^{si}(t\vert t) = \begin{cases} \widehat{SOC}(t+1\vert t), & si = 1 \\ \widehat{SOC}(t+1\vert t) + \left(\sqrt{(1+\lambda)\widehat{P}(t\vert t)}\right), & si = 2 \\ \widehat{SOC}(t+1\vert t) - \left(\sqrt{(1+\lambda)\widehat{P}(t\vert t)}\right), & si = 3 \end{cases}$ where si is the order of sigma points. Normally, the UKF utilizes the $2L+1$ sigma points, where L is the number of estimated states. In this paper, $L = 1$, so we have three sigma points and the length of $\widehat{X}(t\vert t)$ is 3. $si = 1$ indicates the first sigma point, $si = 2$ indicates the second sigma point, and $si = 3$ indicates the third sigma point, $\widehat{P}(t\vert t)$ is the posteriori state estimation error covariance matrix for the previous time interval. $\widehat{SOC}(t+1\vert t)$ is the posteriori state estimation for the previous time interval. λ is a constant that describes the distance between the sigma point and the mean point. The mean weight $W_m^{(si)}$ and variance weight $W_c^{(si)}$ are defined as: $W_m^{(si)} = \begin{cases} \frac{\lambda}{1+\lambda}, & si = 1 \\ \frac{1}{2(1+\lambda)}, & si \neq 1 \end{cases}$ $W_c^{(si)} = \begin{cases} \frac{\lambda}{1+\lambda} + (1 - \alpha^2 + \beta), & si = 1 \\ \frac{1}{2(1+\lambda)}, & si \neq 1 \end{cases}$ where $\lambda = \alpha^2(1+\kappa) - 1$, and $\alpha \in [0, 1]$. In a normal distribution, $\beta = 2$ and $\kappa = 0$.
7	**Priori state estimation:** $\widehat{X}^{si}(t+1\vert t) = \widehat{X}^{si}(t\vert t) + I * \Delta t / Q_{capacity}$ $\widehat{SOC}(t+1\vert t) = \sum_{si=1}^{3} W_m^{(si)} \widehat{X}^{si}(t+1\vert t)$
8	**Project the error covariance ahead:** $\widehat{P}(t+1\vert t) = \sum_{si=1}^{3} W_m^{(si)} \left(\widehat{X}^{si}(t+1\vert t) - \widehat{SOC}(t+1\vert t)\right) \cdot$ $\left(\widehat{X}^{si}(t+1\vert t) - \widehat{SOC}(t+1\vert t)\right)^T + Q_{pnc}$ where Q is the covariance of the process noise.
9	**Estimate the output** DQV: $DQV_{pulse}(\widehat{SOC}(t+1\vert t)) = \sum_{si=1}^{3} W_m^{(si)} DQV_{complete}(\widehat{X}^{si}(t+1\vert t))$
10	**Estimate the covariance of the measurement** P_y **and the covariance between the measurement and the state** P_{xy}: $P_y = \sum_{si=1}^{3} W_c^{(si)} \left(W_m^{(si)} DQV_{complete}(\widehat{X}^{si}(t+1\vert t)) - DQV_{pulse}(\widehat{SOC}(t+1\vert t))\right) \cdot$ $\left(W_m^{(si)} DQV_{complete}(\widehat{X}^{si}(t+1\vert t)) - DQV_{pulse}(\widehat{SOC}(t+1\vert t))\right)^T + R_{mnc}$ $P_{xy} = \sum_{si=1}^{3} W_c^{(si)} \left(\widehat{X}^{si}(t+1\vert t) - \widehat{SOC}(t+1\vert t)\right) \cdot$ $\left(W_m^{(si)} DQV_{complete}(\widehat{X}^{si}(t+1\vert t)) - DQV_{pulse}(\widehat{SOC}(t+1\vert t))\right)^T$
11	**Compute the Kalman filter gain:** $K(t+1) = P_{xy} P_y^{-1}$
12	**Update the state estimate using the measurement model prediction error:** $\widehat{SOC}(t+1\vert t+1) = \widehat{SOC}(t+1\vert t) + K(t+1)\left(DQV_{pulse}(t+1) - DQV_{pulse}(\widehat{SOC}(t+1\vert t))\right)$
13	**Update the covariance of the state variables:** $\widehat{P}(t+1\vert t+1) = \widehat{P}(t+1\vert t) - K(t+1) P_y K^T(t+1)$
14	**End for**

CRediT authorship contribution statement

Yizhao Gao: Writing – original draft, Validation, Methodology, Formal analysis, Data curation, Conceptualization. **Simona Onori:** Writing – review & editing, Project administration, Funding acquisition.

Declaration of competing interest

The authors declare that they have no known competing financial interests or personal relationships that could have appeared to influence the work reported in this paper.

Acknowledgments

The authors acknowledge the partial financial support of National Science Foundation (NSF), United States through the CAREER Award number CMMI-1839050, and also acknowledge the partial financial support from the EIC laboratories. The authors also would like to thank Stanford Energy Control Lab members Simone Fasolato, Joseph Lucero, and Muhammad Aadil Khan for providing helpful comments on this manuscript.

Appendix

See Table 4.

Data availability

Data will be made available on request.

References

[1] Padhi Akshaya K, Nanjundaswamy Kirakodu S, Goodenough John B. Phospho-olivines as positive-electrode materials for rechargeable lithium batteries. J Electrochem Soc 1997;144(4):1188.

[2] Jokar Ali, Désilets Martin, Lacroix Marcel, Zaghib Karim. Mesoscopic modeling and parameter estimation of a lithium-ion battery based on LiFePO4/graphite. J Power Sources 2018;379:84–90.

[3] Plett Gregory L. Extended Kalman filtering for battery management systems of LiPB-based HEV battery packs: Part 1. Background. J Power Sources 2004;134(2):252–61, URL https://www.sciencedirect.com/science/article/pii/S0378775304003593.

[4] Plett Gregory L. Extended Kalman filtering for battery management systems of LiPB-based HEV battery packs: Part 3. State and parameter estimation. J Power Sources 2004;134(2):277–92, URL https://www.sciencedirect.com/science/article/pii/S0378775304003611.

[5] Plett Gregory L. Sigma-point Kalman filtering for battery management systems of LiPB-based HEV battery packs: Part 1: Introduction and state estimation. J Power Sources 2006;161(2):1356–68, URL https://www.sciencedirect.com/science/article/pii/S0378775306011414.

[6] Zhang Zhihang, Li Yalun, Wang Hewu, Lu Languang, Han Xuebing, Li Desheng, Ouyang Minggao. A comparative study of the LiFePO4 battery voltage models under grid energy storage operation. J Energy Storage 2024;75:109696, URL https://www.sciencedirect.com/science/article/pii/S2352152X23030943.

[7] Li Jiahao, Klee Barillas Joaquin, Guenther Clemens, Danzer Michael A. A comparative study of state of charge estimation algorithms for LiFePO4 batteries used in electric vehicles. J Power Sources 2013;230:244–50, URL https://www.sciencedirect.com/science/article/pii/S0378775312019039.

[8] Gao Yizhao, Nguyen Trung, Onori Simona. Model-based state-of-charge estimation of 28 V LiFePO 4 aircraft battery. SAE Int J Electrified Veh 2024;14(14-14-01-0003).

[9] Zhu Guorong, Wu Oukai, Wang Qian, Kang Jianqiang, Wang Jing V. The modeling and SOC estimation of a LiFePO4 battery considering the relaxation and overshoot of polarization voltage. Batteries 2023;9(7). URL https://www.mdpi.com/2313-0105/9/7/369.

[10] Lai Xin, Sun Lin, Chen Quanwei, Wang Mingzhu, Chen Junjie, Ke Yuehang, Zheng Yuejiu. A novel modeling methodology for hysteresis characteristic and state-of-charge estimation of LiFePO4 batteries. J Energy Storage 2024;101:113807, URL https://www.sciencedirect.com/science/article/pii/S2352152X24033930.

[11] Wang Guan, Jin Bei, Wang Mingzhu, Sun Yuedong, Zheng Yuejiu, Su Teng. State of charge estimation for "LiFePO4-LiCoxNiyMn1-x-yo2" hybrid battery pack. J Energy Storage 2023;65:107345.

[12] Xiong Rui, Duan Yanzhou, Zhang Kaixuan, Lin Da, Tian Jinpeng, Chen Cheng. State-of-charge estimation for onboard LiFePO4 batteries with adaptive state update in specific open-circuit-voltage ranges. Appl Energy 2023;349:121581.

[13] Chun Chang Yoon, Cho BH, Kim Jonghoon. Covariance controlled state-of-charge estimator of LiFePO4 cells using a simplified hysteresis model. Electrochim Acta 2018;265:629–37.

[14] Peng Simin, Zhang Daohan, Dai Guohong, Wang Lin, Jiang Yuxia, Zhou Feng. State of charge estimation for LiFePO4 batteries joint by PID observer and improved EKF in various OCV ranges. Appl Energy 2025;377:124435, URL https://www.sciencedirect.com/science/article/pii/S030626192401818X.

[15] Ko Younghwi, Choi Woojin. A new soc estimation for lfp batteries: Application in a 10 ah cell (hw 38120 l/s) as a hysteresis case study. Electronics 2021;10(6):705.

[16] Chen Cheng, Xiong Rui, Yang Ruixin, Li Hailong. A novel data-driven method for mining battery open-circuit voltage characterization. Green Energy Intell Transp 2022;1(1):100001.

[17] Li Junfu, Lai Qingzhi, Wang Lixin, Lyu Chao, Wang Han. A method for SOC estimation based on simplified mechanistic model for LiFePO4 battery. Energy 2016;114:1266–76.

[18] Koga Shumon, Camacho-Solorio Leobardo, Krstic Miroslav. State estimation for lithium-ion batteries with phase transition materials via boundary observers. J Dyn Syst Meas Control 2021;143(4):041004.

[19] Gao Yizhao, Plett Gregory L, Fan Guodong, Zhang Xi. Enhanced state-of-charge estimation of LiFePO4 batteries using an augmented physics-based model. J Power Sources 2022;544:231889.

[20] Wei Meng, Ye Min, Zhang Chuawei, Lian Gaoqi, Xia Baozhou, Wang Qiao. Robust state of charge estimation of LiFePO4 batteries based on sage_husa adaptive Kalman filter and dynamic neural network. Electrochim Acta 2024;477:143778.

[21] Tian Jinpeng, Xiong Rui, Shen Weixiang, Lu Jiahuan. State-of-charge estimation of LiFePO4 batteries in electric vehicles: A deep-learning enabled approach. Appl Energy 2021;291:116812.

[22] Che Yunhong, Xu Le, Teodorescu Remus, Hu Xiaosong, Onori Simona. Enhanced SOC estimation for LFP batteries: A synergistic approach using Coulomb counting reset, machine learning, and relaxation. ACS Energy Lett 2025;10:741–9.

[23] Beltran Hector, Sansano Emilio, Pecht Michael. Machine learning techniques suitability to estimate the retained capacity in lithium-ion batteries from partial charge/discharge curves. J Energy Storage 2023;59:106346.

[24] Fly Ashley, Chen Rui. Rate dependency of incremental capacity analysis (dQ/dV) as a diagnostic tool for lithium-ion batteries. J Energy Storage 2020;29:101329.

[25] Spitthoff Lena, Vie Preben JS, Wahl Markus Solberg, Wind Julia, Burheim Odne Stokke. Incremental capacity analysis (dQ/dV) as a tool for analysing the effect of ambient temperature and mechanical clamping on degradation. J Electroanal Chem 2023;944:117627.

[26] Wang Yujie, Li Kaiquan, Peng Pei, Chen Zonghai. Health diagnosis for lithium-ion battery by combining partial incremental capacity and deep belief network during insufficient discharge profile. IEEE Trans Ind Electron 2023;70(11):11242–50.

[27] Bian Xiaolei, Wei Zhongbao, He Jiangtao, Yan Fengjun, Liu Longcheng. A novel model-based voltage construction method for robust state-of-health estimation of lithium-ion batteries. IEEE Trans Ind Electron 2021;68(12):12173–84.

[28] Novak Matej, Mikolasek Miroslav. State of health estimation of lithium-ion batteries based on incremental capacity and pulse analysis. In: 2023 13th European space power conference. ESPC, IEEE; p. 1–6.

[29] Yu Kun, Wang Hang, Mao Lei, He Qingbo, Wu Qiang. IC curve-based lithium-ion battery SOC estimation at high rate charging current. IEEE Trans Instrum Meas 2022;71:1–9.

[30] Liu Guangming, Ouyang Minggao, Lu Languang, Li Jianqiu, Han Xuebing. Online estimation of lithium-ion battery remaining discharge capacity through differential voltage analysis. J Power Sources 2015;274:971–89.

[31] Zheng Linfeng, Zhu Jianguo, Lu Dylan Dah-Chuan, Wang Guoxiu, He Tingting. Incremental capacity analysis and differential voltage analysis based state of charge and capacity estimation for lithium-ion batteries. Energy 2018;150:759–69.

[32] Lin CP, Cabrera Javier, Denis YW, Yang Fangfang, Tsui KL. SOH estimation and SOC recalibration of lithium-ion battery with incremental capacity analysis & cubic smoothing spline. J Electrochem Soc 2020;167(9):090537.

[33] Wang Limei, Pan Chaofeng, Liu Liang, Cheng Yong, Zhao Xiuliang. On-board state of health estimation of LiFePO4 battery pack through differential voltage analysis. Appl Energy 2016;168:465–72.

[34] Catenaro Edoardo, Onori Simona. Experimental data of lithium-ion batteries under galvanostatic discharge tests at different rates and temperatures of operation. Data Brief 2021;35:106894.

[35] Gao Yizhao, Onori Simona. Systems and methods for state-of-charge estimation based on dQ/dV curve. 2025, https://patentscope.wipo.int/search/en/WO2025122659.

[36] Plett Gregory L. Battery management systems, Volume II: Equivalent-circuit methods. Artech House; 2015.

[37] MathWorks. SOC Estimator (Kalman Filter). 2024, URL https://www.mathworks.com/help/simscape-battery/ref/socestimatorkalmanfilter.html, [Accessed 04 May 2025].

[38] Ha Sara, Pozzato Gabriele, Onori Simona. Electrochemical characterization tools for lithium-ion batteries. J Solid State Electrochem 2023;1–27, Springer.